Shedding Light on Cardiac Excitation: In Vitro and In Silico Analysis of Native Ca2+ Channel Activation in Guinea Pig Cardiomyocytes using Organic Photovoltaic Devices

Rienmüller, Theresa; Shrestha, Niroj; Polz, Mathias; Stoppacher, Sara; Ziesel, Daniel; Migliaccio, Ludovico; Pelzmann, Brigitte; Lang, Petra; Zorn-Pauly, Klaus; Langthaler, Sonja; ...

Source / Izvornik: **IEEE Transactions on Biomedical Engineering, 2024, 71, 1980 - 1992**

Journal article, Published version
Rad u časopisu, Objavljena verzija rada (izdavačev PDF)

https://doi.org/10.1109/TBME.2024.3358240

Permanent link / Trajna poveznica: https://urn.nsk.hr/urn:nbn:hr:217:445483

Shedding Light on Cardiac Excitation: In Vitro and In Silico Analysis of Native Ca^{2+} Channel Activation in Guinea Pig Cardiomyocytes Using Organic Photovoltaic Devices

Theresa Rienmüller, Niroj Shrestha, Mathias Polz, Sara Stoppacher, Daniel Ziesel, Ludovico Migliaccio, Brigitte Pelzmann, Petra Lang, Klaus Zorn-Pauly, Sonja Langthaler, Aleksandar Opančar, Christian Baumgartner, Muammer Üçal, Rainer Schindl, Vedran Đerek, and Susanne Scheruebel

Abstract*—*Objective: **This study aims to explore the potential of organic electrolytic photocapacitors (OEPCs), an innovative photovoltaic device, in mediating the activation of native voltage-gated Cav1.2 channels ($I_{Ca,L}$) in Guinea pig ventricular cardiomyocytes. *Methods:* Whole-cell patch-clamp recordings were employed to examine light-triggered OEPC mediated $I_{Ca,L}$ activation, integrating the channel's kinetic properties into a multicompartment cell model to take intracellular ion concentrations into account. A multidomain model was additionally incorporated to evaluate effects of OEPC-mediated stimulation. The final model combines external stimulation, multicompartmental cell simulation, and a patch-clamp amplifier equivalent circuit to assess the impact on achievable intracellular voltage changes. *Results:* Light pulses activated $I_{Ca,L}$, with amplitudes similar to voltage-clamp activation and high sensitivity to the L-type Ca^{2+} channel blocker, nifedipine. Light-triggered $I_{Ca,L}$ inactivation exhibited kinetic parameters comparable to voltage-induced inactivation. *Conclusion:* OEPC-mediated activation of $I_{Ca,L}$ demonstrates their potential for nongenetic optical modulation of cellular physiology potentially paving the way for the development of innovative therapies in cardiovascular health. The integrated model proves the light-mediated activation of $I_{Ca,L}$ and advances the understanding of the interplay between the patch-clamp amplifier and external stimulation devices. *Significance:* Treating cardiac conduction disorders by minimal-invasive means without genetic modifications could advance therapeutic approaches increasing patients' quality of life compared with conventional methods employing electronic devices.**

***Index Terms*—Biomedical modeling and simulation, calcium, cardiac physiology, electrophysiology, optoelectronic devices, patch-clamp, voltage-gated ion channels.**

Manuscript received 22 August 2023; revised 19 December 2023; accepted 12 January 2024. Date of publication 18 March 2024; date of current version 13 May 2024. The work of Muammer Üçal, Mathias Polz, Susanne Scheruebel, Daniel Ziesel, and Theresa Rienmüller was supported in part by Austrian Science Fund (Zukunftskolleg ZK17). The work of Vedran Đerek was supported in part by Croatian Government through Project CeNIKS cofinanced, in part by European Union through European Regional Development Fund – Competitiveness and Cohesion Operational Programme under Grant KK.01.1.1.02.0013, and in part by the QuantiXLie Center of Excellence, a project co-financed by Croatian Government and European Union through the European Regional Development Fund – the Competitiveness and Cohesion Operational Programme under Grant KK.01.1.1.01.0004. This work was supported by Croatian Science Foundation under Grant UIP-2019-04-1753. *(Theresa Rienmüller and Niroj Shrestha contributed equally this work.) (Corresponding authors: Theresa Rienmüller; Vedran Đerek; Susanne Scheruebel.)*

Theresa Rienmüller is with the BioTechMed-Graz, 8010 Graz, Austria, and also with the Institute of Healthcare Engineering with European Testing Center of Medical Devices, Graz University of Technology, A-8010 Graz, Austria (e-mail: theresa.rienmueller@tugraz.at).

Niroj Shrestha, Petra Lang, and Klaus Zorn-Pauly are with the Gottfried Schatz Research Center for Cell Signaling, Metabolism and Aging, Medical Physics and Biophysics, Medical University of Graz, Austria.

Mathias Polz, Daniel Ziesel, and Sonja Langthaler are with the Institute of Healthcare Engineering with European Testing Center of Medical Devices, University of Technology, Austria.

Sara Stoppacher is with BioTechMed-Graz, Austria, and also with Institute of Healthcare Engineering with European Testing Center of Medical Devices, Graz University of Technology, Austria.

Ludovico Migliaccio is with the Bioelectronics Materials and Devices Laboratory, Brno University of Technology, Czech Republic.

Brigitte Pelzmann is with the Gottfried Schatz Research Center for Cell Signaling, Metabolism and Aging, Medical Physics and Biophysics, Medical University of Graz, Austria, and also with BioTechMed-Graz, Austria.

Aleksandar Opančar is with the Department of Physics, Faculty of Science, University of Zagreb, Croatia.

Christian Baumgartner is with the Institute of Healthcare Engineering with European Testing Center of Medical Devices, Graz University of Technology, Austria, and also with BioTechMed-Graz, Austria.

Muammer Üçal is with the Research Unit of Experimental Neurotraumatology, Department of Neurosurgery, Medical University of Graz, Austria, and with the Department of Neurology, Medical University of Graz, Austria, and also with BioTechMed-Graz, Austria.

Rainer Schindl is with the Gottfried Schatz Research Center for Cell Signaling, Metabolism and Aging, Medical Physics and Biophysics, Medical University of Graz, Austria, and also with BioTechMed-Graz, Austria.

Vedran Đerek is with the Department of Physics, Faculty of Science, University of Zagreb, 10363 Zagreb, Croatia (e-mail: vedran.derek@pmf.hr).

Susanne Scheruebel is with the Gottfried Schatz Research Center for Cell Signaling, Metabolism and Aging, Medical Physics and Biophysics, Medical University of Graz 8010 Graz, Austria (e-mail: susanne.scheruebel@medunigraz.at).

Digital Object Identifier 10.1109/TBME.2024.3358240

I. Introduction

THE use of bioelectronics to modulate physiological processes has opened up a plethora of possibilities, ranging from fundamental research to clinical applications as medical implants [1], [2], [3]. Electrical stimulation can be applied via neuromodulation devices [4] such as retinal [5] and cochlear implants or electrodes implanted in the brain such as deep brain stimulation [6]. The use of such devices involves direct contact

between electrodes and tissue and often requires additional wires connected to an external power supply [7], [8].

Alternative wireless methods to stimulate excitable cells encompass a range of approaches, including optogenetics, photothermal stimulation using materials with strong absorption in the near-infrared spectrum, and photomechanical stimulation, where light induces physical changes in materials to generate mechanical forces [9]. Additionally, optical stimulation using a nanowire matrix or infrared laser pulses has been employed proving successful in evoking contractions in native neonatal rat cardiomyocytes or quail hearts [10]. By means of a free standing polymer-silicon nanowire mesh including laser input the authors were able to stimulate neonatal rat cardiomyocytes and adult rat hearts ex vivo to beat with a targeted frequency [9]. While optogenetics also enables wireless photostimulation, it necessitates genetic modification of the stimulated tissue [11], making the in vivo implementation challenging, hence limiting its clinical application. In contrast, optoelectronic devices based on conventional inorganic semiconductors such as silicon offer wireless and nongenetic platforms for effective photostimulation of excitable cells such as neurons [12]. Thickness and rigidity, however, constitute two major limitations of silicon-based devices for their use in soft and sensitive tissue [13]. Considering these drawbacks, we use the recently developed organic electrolytic photocapacitors (OEPCs) as promising wireless, nongenetic, and biocompatible devices for extracellular photostimulation with high temporal precision and short latency [14], [15]. OEPCs consist of an ultrathin, transparent donor-acceptor bilayer of metal-free hydrogen-bonded pigments, phthalocyanine (H_2Pc, p-type), and N,N′-dimethylperylene-34,910-tetracarboxylic diimide (PTCDI, n-type), deposited on top of a conductive transparent back electrode such as indium tin oxide (ITO). These photosensitive pigments are cheap, nontoxic, and commercially used in cosmetics, outdoor paints, and printing inks [16]. They have higher absorption coefficients than silicon, thereby allowing the OEPCs' active layer to be fabricated with a thickness of only tens of nanometers resulting in flexible and minimally invasive devices when used in combination with thin film substrates [15]. In our previous in vitro studies, we established OEPCs as extracellular predominantly capacitive stimulation electrodes. They absorb light in the visible spectrum, mainly within a wavelength range of 630–660 nm, and generate ionic currents in physiological solution at the semiconductor/electrolyte and back electrode/electrolyte interfaces of the oppositely charged double layers. Here, capacitive charging current on the photoactive layer has cathodic polarity when the light pulse begins and discharging current has opposite polarity when the light pulse ends so that the optical on/off square light pulse is transduced into a biphasic capacitive cathodic-leading pulse. The transducive extracellular potential generated between the OEPC's n-layer and the cell [17] can depolarize a cell membrane in close contact or adhered to its surface [18]. This depolarization was shown to activate heterologously expressed, voltage-gated potassium channels K_v1.3 in *Xenopus laevis* oocytes [15] and human embryonic kidney cells [19], and to stimulate blind retinas explanted from chicken embryos 100 times below the safe limit for ocular stimulation [14]. Light of a 630–660 nm wavelength range lies within the tissue transparency window and safely penetrates skin, muscle, and even bone at limited intensities [20]. Predominant photothermal or faradaic stimulation, on the other hand, may damage cells or tissues by generating heat or reactive oxygen species [21], [22]. In further studies, a thin coat of conducting polymer poly(34-ethylenedioxythiophene):polystyrene sulfonate (PEDOT:PSS) on top of either the entire device or only the back electrode was shown to enhance the capacitive charge density while reducing the interfacial impedance of the stimulating photoelectrode [15], [19]. Flexible OEPC devices have also been implanted in rodents to photostimulate peripheral nerves and somatosensory cortex tissue in vivo [24], [25]. In further studies using photovoltaic devices, Abdullaeva et al. reported the activation of I_{Na} and I_K in neuroblastoma cells via photocapacitive and photothermal effects induced by organic heterojunctions using blended photoactive materials [26].

However, the complex activation and inactivation kinetics of membrane currents via endogenous voltage-gated and ion-regulated ion channels in larger excitable mammalian cells such as cardiac myocytes when subjected to stimulation from OEPC devices have not been explored so far. Recognizing the important role of intracellular calcium in cardiac electrical conduction, our study aims to investigate the activation/inactivation of Ca^{2+} current via native voltage-gated Ca_v1.2 channels ($I_{Ca,L}$) in primary cultures of Guinea pig ventricular myocytes on OEPCs. The outline of this work is as follows. To ensure that the OEPC surface does not influence the behavior of the cells, we first assess $I_{Ca,L}$ activation in cardiac cells on OEPC devices by depolarizing the membrane using voltage-clamp protocols and compare the results to previous voltage-clamp recordings on a glass substrate. Next, we use activation and inactivation protocols with either light pulses or voltage steps in voltage-clamp experiments. Nifedipine, an L-type Ca^{2+} channel blocker, is used to confirm the light-triggered activation of $I_{Ca,L}$ in the experiments. Using a comprehensive mathematical model of the cardiac cell, the membrane voltages and ion channel currents obtained from the patch-clamp system in combination with external stimulation are compared with the conventional voltage clamp recordings. $I_{Ca,L}$ gating is both voltage and Ca^{2+} dependent, and $I_{Ca,L}$-mediated Ca^{2+} influx triggers Ca^{2+} release from the sarcoplasmic reticulum (SR) through ryanodine receptor (RyR) clusters inside the dyadic clefts [27]. Thus, modeling the calcium dynamics of cardiac myocytes requires a detailed description of both the dyadic structure and the whole-cell membrane currents. Our model, therefore, includes a description of individual ion currents and spatially detailed concentration dynamics in dyadic clefts, SR, and bulk myoplasm [28]. This multicompartmental model is combined with a two-domain model describing the effect of external stimulation [18], [19], [29] taking the relative size of the cell and the stimulation electrode and the looser coupling and thus the larger cleft between the cell and the OEPC device into account. A detailed model of the patch-clamp amplifier circuit is defined to account for artifacts arising from the light-triggered stimulation and the patch-clamp amplifier circuit, comprising series resistance, membrane and pipette capacitance, as well as compensations made by the amplifier for these phenomena [30], and, especially, in response to the external stimulus.

II. Materials and Methods

A. OEPC Fabrication

OEPCs were fabricated as described previously with small modifications [19]. In brief, polyterephthalate (PET) foils coated with indium tin oxide (ITO) (Merck, Germany) were sonicated sequentially in isopropanol, 2% Hellmanex III solution, and deionized water. Finally, the substrates were treated with oxygen plasma (50 W, 2 min, Diener electronic GmbH). The substrates were then exposed to n-octyltriethoxysilane (OTS) vapor in a steel Petri dish heated to 90 °C for 1 h. The samples were subsequently sonicated in acetone and washed with isopropanol and deionized water to remove multilayers of OTS. The OTS treatment was patterned by PVC adhesive tape. Next, the organic semiconductors phthalocyanine H_2Pc (Alfa Aesar) and *N,N′*-dimethyl-34,910-perylenetetracarboxylic diimide (PTCDI) (BASF), both purified by three-fold temperature-gradient sublimation, were deposited in a PVD chamber through a PVC adhesive tape mask. The process was done at $<2 \times 10^{-6}$ Torr, a rate of 1–5 $Å s^{-1}$, and 30 nm of each material were successively evaporated to produce seven organic semiconductor pixels (PN) of 13 mm diameter. The thermal control (indigo, BASF) samples were processed similarly, except that the evaporated layer was 60 nm thick to offset the higher absorption coefficient of the phthalocyanine absorber. The devices were then coated with poly(34-ethylenedioxythiophene):polystyrene sulfonate (PEDOT:PSS) solution. PEDOT:PSS (Clevios PH 1000, Heraeus) and 3-glycidoxypropyltrimethoxysilane (2% v/v) were sonicated together for 10 min and spin-coated (5000 rpm, 30 s) all over the PN and ITO layer. The PEDOT:PSS devices were then annealed at 120 °C for 90 min. Finally, all devices were tested for functionality with the electrophotoresponse technique as previously described [19] and PET foil with PN and surrounding ITO was cut to 25 mm diameter to produce seven OEPC devices.

B. Animals

The experimental procedure and the number of animals used were approved by the ethics committee of the Federal Ministry of Science, Research and Economy of the Republic of Austria (BMWF-66.010/0110-WF/V/3b/2016). The experiments were conducted according to the Directive of the European Parliament and of the Council of September 22, 2010 (2010/63/EU). 6–10-week-old Dunkin Hartley Guinea pigs (Charles River Laboratories, Sulzfeld, Germany) of either sex were used.

C. Reagents

All reagents used were of molecular biology grade and purchased from Merck or Carl Roth unless specified otherwise.

D. Isolation of Guinea Pig Ventricular Myocytes

Ventricular myocytes were isolated from Guinea pigs as described previously [31]. Guinea pigs were deeply anesthetized with an intraperitoneal injection of 40 mg/kg ketamine (aniMedica GmbH, Germany) and 10 mg/kg xylazine (Bayer GmbH, Austria). Hearts were quickly excised, mounted on a Langendorff apparatus and the coronary system was perfused with a buffer (composition in mM: 126 NaCl, 4.7 KCl, 1.2 KH_2PO_4, 2.5 $MgSO_4$, 2.49 $NaHCO_3$, 0.5 HEPES/Na^+, and 5.45 D(+)-glucose, pH 7.4 adjusted with NaOH) containing 2 mM pyruvic acid, 1 mg/ml bovine serum albumin, and 100 IU/ml collagenase (Worthington Biochemical Corporation, NJ, USA) at 37 °C. After enzymatic digestion for 25–30 min, myocytes were isolated from ventricles using a Pasteur pipette and Ca^{2+} concentration was raised stepwise to 1.8 mM. Cells were transferred to M199 medium supplemented with 5% fetal bovine serum, 2 mM L-glutamine, 50 IU/ml penicillin and 50 μg/ml streptomycin, and incubated at 37 °C under 5% CO_2.

E. Electrophysiological Recordings

Electrophysiological recordings were performed one day after isolation in the whole-cell single-electrode voltage-clamp configuration using Axopatch 200B amplifier connected to Digidata 1550B interface and Clampex v11.1 software (Molecular Devices, Germany) [31]. A few drops of medium containing myocytes were transferred on an OEPC device mounted in a perfusion chamber on an inverted microscope (Zeiss Axiovert 135, Germany) with a 32x/0.4 objective and perfused with an external solution (containing in mM: 137 NaCl, 5.4 CsCl, 1.8 $CaCl_2$, 1.1 $MgCl_2$, 2.2 $NaHCO_3$, 0.4 NaH_2PO_4, 10 HEPES/Na^+, 5.6 D(+)-glucose, adjusted to pH 7.4 with NaOH) at a flow rate of ∼3 ml/min at 37 °C. Only quiescent, rod-shaped myocytes with clear cross-striations were patched with patch pipettes filled with internal solution (containing in mM: 110 CsCl, 4.3 ATP/Na^+, 2 $MgCl_2$, 1 $CaCl_2$, 11 EGTA, and 10 HEPES/Cs^+, adjusted to pH 7.4 with CsOH) and a tip resistance of 2–3 MΩ. Pipette capacitance was compensated before the recordings. Cell membrane capacitance was measured and calculated as described previously [32]. Whole-cell series resistance was compensated to 40%. In order to allow equilibration of internal solution with the cytosol, current recordings were started 2 min after the rupture of the membrane patch. The current density was calculated by dividing the measured current amplitudes by the cell membrane capacitance and expressed as pA/pF to allow comparison between cells of different sizes.

L-type Ca^{2+} current ($I_{Ca,L}$) was measured and characterized as described previously [31]. In order to study $I_{Ca,L}$ without contamination of Na^+ current, a 100 ms prepulse from a holding potential of −80 mV to −40 mV was used to activate and voltage-inactivate Na^+ current. K^+ currents were suppressed by substituting K^+ with Cs^+ ions in the external and internal solutions. $I_{Ca,L}$ was elicited by a train of voltage pulses from −40 to +90 mV (10 mV interval, 100 ms) and the current amplitude was calculated as the difference between the peak inward current and the current at the end of the pulse. Steady-state activation of $I_{Ca,L}$ was obtained by dividing the peak values of $I_{Ca,L}$ with the driving force to compute the $I_{Ca,L}$ conductance ($g_{Ca,L}$), normalized with the maximum value and plotted against the

voltage pulse. Curves were fitted according to the Boltzmann equation

$$d_\infty = \frac{1}{\left[1+\exp\left\{\left(V_{1/2\text{activation}}-V\right)/k\right\}\right]}, \quad (1)$$

where V is the membrane potential, $V_{1/2\text{activation}}$ is the membrane potential of half maximum activation and k is the slope of the activation curve.

To directly compare voltage-clamp activation with light-mediated channel opening, $I_{\text{Ca,L}}$ was further measured in the same cell using 100 ms $\lambda_{660\ \text{nm}}$ light pulses with 10 mW/mm^2 at -40 mV instead of a depolarizing voltage pulse. In order to prove the contribution of $I_{\text{Ca,L}}$ to the measured current, measurements were carried out with a voltage-clamp step protocol from -40 mV to different voltage levels or a $\lambda_{660\ \text{nm}}$ light pulse (100 ms) before and after 1 min superfusion with 30 μM nifedipine, an L-type Ca^{2+} channel blocker. To determine steady-state inactivation, $I_{\text{Ca,L}}$ was activated with test pulses to +10 mV or $\lambda_{660\ \text{nm}}$ light pulses with a length of 100 ms, preceded by conditioning pulses from −45 to +10 mV (5 mV increment, 400 ms) from a holding potential of −45 mV. $I_{\text{Ca,L}}$ amplitude elicited by the test pulse was normalized to the maximum value and plotted as a function of prepulse potential. Curves were again fitted using the Boltzmann function

$$f_\infty = \frac{1}{\left[1+\exp\left\{\left(V-V_{1/2\text{activation}}\right)/k\right\}\right]}, \quad (2)$$

where V is the command membrane potential, $V_{1/2\text{inactivation}}$ is the command membrane potential of half maximum inactivation and k is the slope of the inactivation curve.

F. Statistical Analysis and Figures

Electrophysiological data were analyzed in GraphPad Prism v8.4.3 (GraphPad Software, USA) and plotted using OriginPro 2018 (OriginLab Corporation, USA). N represents the number of cells unless specified otherwise. The normal distribution of the data was confirmed by the z-value of skewness and kurtosis between −1.96 and +1.96, and the Shapiro-Wilk test. Statistical significance of the differences observed between two groups was analyzed using unpaired t-test and plotted as mean ± SEM unless specified otherwise. All tests were two-tailed and the differences with a p value < 0.05 were deemed statistically significant.

The plots for the Figures were in part created with BioRender.com.

G. Cell Model

Cell behavior was modeled based on the theoretical LRd model of a mammalian ventricular cell, with parameters mostly chosen from Guinea pig ventricular myocyte experimental data [33]. The model includes membrane ion channels, pumps, and exchangers, and takes changes in intracellular ion concentration into account. The K^+ channels, the Na^+-K^+ pump, and internal changes of K^+ concentrations were omitted since K^+ currents were suppressed by substituting K^+ with Cs^+ ions in the external and internal solutions (see Fig. 1) and instead replaced by a background current I_b. In our model, we focus on the voltage- and Ca^{2+}-gated activation and inactivation of cardiac $I_{\text{Ca,L}}$. We follow the idea of a multicompartmental model for the internal Ca^{2+} concentrations [34] i.e., the modeled cell is divided into subvolumes, the junctional SR (JSR) and the network SR (NSR), the bulk myoplasm, and the dyadic space. When Ca^{2+} enters myoplasm via cardiac L-type Ca^{2+} channels or release from the SR, it results in higher local Ca^{2+} concentrations near the inner membrane surface than in the bulk myoplasm. This, in turn, causes Ca^{2+}-induced Ca^{2+} release through ryanodine receptor channels (I_{rel}), which are present in the JSR membrane facing the dyadic clefts [27], [33], [34]. Different ionic concentrations are thus modeled for each compartment Ca_{NSR}, Ca_{JSR}, Ca_{d}, Ca_{i}, depending on the respective volumes, Ca^{2+} diffusion rates from the dyadic cleft to the bulk myoplasm, Ca^{2+}-entry via $I_{\text{Ca,L}}$, and I_{rel}, and the amount of Ca^{2+} leaving through the Na^+-Ca^{2+} exchanger (I_{NaCa}, and $I_{\text{NaCa,ss}}$).

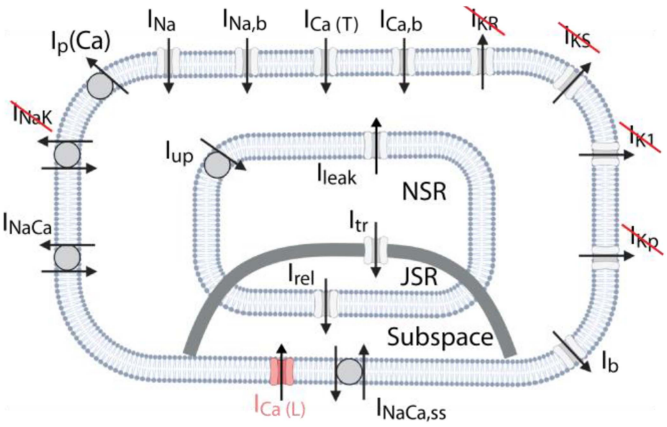

Fig. 1. Multicompartmental cardiac cell model comprising ion channels, pumps, and exchangers. Different ionic concentrations are modeled for each compartment Ca_{NSR}, Ca_{JSR}, Ca_{d}, Ca_{i} as well as Na_{NSR}, Na_{JSR}, Na_{d}, and Na_{i}. The K^+ currents present in the original are removed and replaced with a background current I_b. Created with BioRender.com.

The current through $I_{\text{Ca,L}}$ is described by (3)

$$I_{\text{Ca,L}} = \bar{P}_{\text{Ca}} \cdot O\left(\text{V}, \left[\text{Ca}^{2+}\right]_{\text{d}}\right) \cdot \delta\left(\text{V}, \left[\text{Ca}^{2+}\right]_{\text{d}}\right), \quad (3)$$

where O is the fraction of open channels [35], which depends on voltage, time, and Ca^{2+}-concentration in the subspace compartment $[Ca^{2+}]_{\text{d}}$ and $\bar{P}_{\text{Ca}}$ is the maximal permeability of the channel for Ca^{2+} ions, scaling the amplitude of the current [36]. δ represents the driving term accounting for the electrochemical forces driving the ionic movement defined by the Goldman-Hodgkin-Katz (GHK) flux (4)

$$\delta = \frac{z_{\text{Ca}}^2 \cdot \text{V} \cdot F^2}{RT} \cdot \frac{\gamma_{\text{Cai}} \cdot \left[Ca^{2+}\right]_{\text{d}} \cdot \exp\left(z_{\text{Ca}} \cdot \text{V} \cdot \frac{F}{RT}\right) - \gamma_{\text{Cao}}\left[Ca^{2+}\right]_o}{\exp\left(z_{\text{Ca}} \cdot \text{V} \cdot F/(RT)\right) - 1}. \quad (4)$$

The channel is slightly permeable for Na^+ and K^+, with a relative permeability ratio of P_{Ca}:P_{Na}:P_{K} = 2800:3.5:1 [37]. In our model, we include the Na^+-permeability $\bar{P}_{\text{Na}} = 1.518 \times$

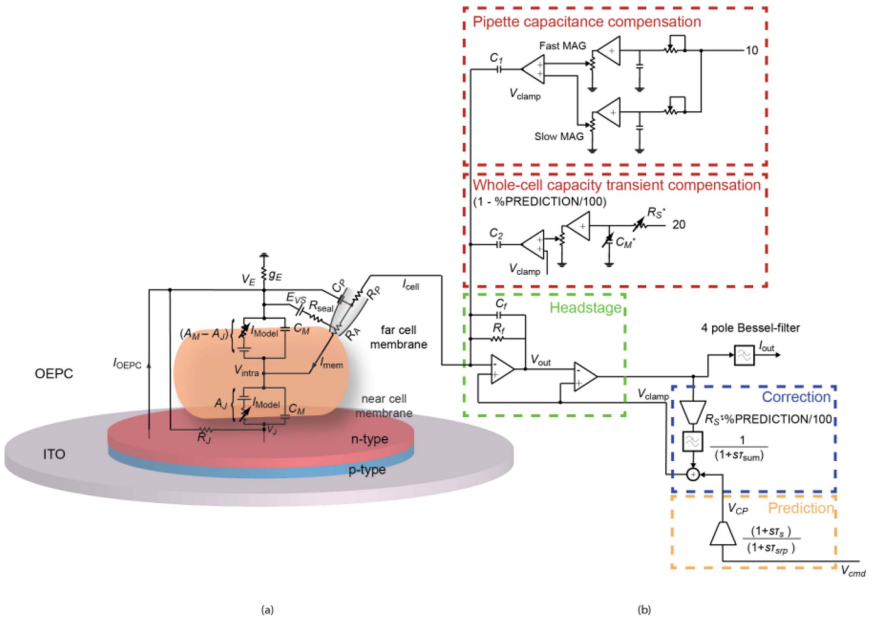

Fig. 2. Equivalent circuit model for the activation of $I_{\mathrm{Ca,L}}$. (a) Model of the cardiac myocyte residing on top of the OEPC device including the artifact components access resistance R_A and pipette resistance R_P, seal resistance R_{SEAL}, and membrane and pipette capacitances C_M and C_P. V_{intra} is the potential controlled/measured by the voltage-clamp amplifier. (b) Patch-clamp amplifier model with feedback elements, compensation circuits, and Bessel output filter.

10^{-6}. The kinetics of the present ion channels are taken from a previous study [33].

H. Mathematical Modeling of External Stimulation and Patch-Clamp Amplifier Circuit

To quantify the effect of OEPC-mediated stimulation on $I_{\mathrm{Ca,L}}$, we implemented a comprehensive model combining the effects of extracellular stimulation with voltage-clamp recordings (see Fig. 2). The model includes a detailed equivalent circuit representation of the patch-clamp amplifier setup including pipette capacitance and whole-cell series resistance compensation, which is crucial to account for artifacts arising in voltage-clamp experiments due to the imperfect properties of the patch-clamp amplifier [30] and to model the capacitive transients that occur in response to external stimulation.

1) Holistic Equivalent Circuit Model for the Patch-Clamp Amplifier: The voltage-clamp measurements were carried out in $\beta = 1$ mode with a specified feedback resistance of $R_{\mathrm{f}} = 500\ \mathrm{M\Omega}$ and a capacitance of $C_{\mathrm{f}} = 1$ pF. The Axopatch 200B uses a dual approach for the correction of errors associated with series resistance R_{S}, i.e., a delayed charging of the membrane capacitance C_{M}, a deviation of the intracellular potential V_{intra} from the command voltage V_{cmd}, when ionic current flows, and a filtering effect on the membrane currents with a corner frequency of $\mathrm{f} = 1/(2\pi R_{\mathrm{S}} C_{\mathrm{M}})$. In order to cancel the whole-cell capacity transient, a current can be injected over the injection capacitance C_2 determined by the setting of both the WHOLE CELL CAP ($C_{\mathrm{M}}*$) and SERIES RESISTANCE ($R_{\mathrm{S}}*$) control. This approach, however, is not sufficient to compensate for the errors described above. The speed by which the intracellular potential changes can be increased using the PREDICTION command, which adds a transient signal to V_{cmd}, increasing the rate at which V_{intra} will change in response to a step voltage command. The command voltage including the PREDICTION transient V_{CP} is then defined as

$$V_{\mathrm{CP}} = V_{\mathrm{cmd}} \cdot \left(\frac{1 + s\tau_{\mathrm{S}}}{1 + s\tau_{\mathrm{SRP}}} \right), \tag{5}$$

with $\tau_{\mathrm{S}} = R_{\mathrm{S}} C_{\mathrm{M}}$, $\tau_{\mathrm{SRP}} = R_{\mathrm{SRP}} C_{\mathrm{M}}$ and $R_{\mathrm{SRP}} = R_{\mathrm{S}}\ (1 - \%\mathrm{PREDICTION}/100)$. The signal applied to the injection capacitor C_2 is modified appropriately by reducing the time constant of this signal as %PREDICTION is increased to $\tau_{\mathrm{inj}} = R_{\mathrm{S}} * C_{\mathrm{M}} * (1 - \%\mathrm{PREDICTION}/100)$. The %CORRECTION setting is finally used to feedback a portion of the measured membrane current in order to compensate for voltage drops across R_{S} and the filtering effects described above. The signal is filtered using a first-order low-pass filter with a time constant of $\tau_{\mathrm{sum}} = \mathrm{LAG}$ prior to being summed with V_{CP}.

The pipette capacitance compensation and membrane capacitance compensation were implemented following descriptions in the vendor's manual [38], with estimated values for the membrane capacitance compensation $C_{\mathrm{M}}*$ and the series resistance compensation $R_{\mathrm{S}}*$ as well as $C_{\mathrm{P}}*$ and $R_{\mathrm{P}}*$ for the pipette capacitance and resistance, respectively.

The total cell membrane current in the model I_{mem} is composed of the capacitive current I_{CM} caused by the capacitive nature of the cell membrane represented in the model by C_{M} and the implemented cell model current I_{model} (see Fig. 1) for the Ca^{2+} and Na^{+} currents present in Guinea pig ventricular myocytes and a background leakage current I_{b}. Furthermore, a capacitive current to charge the pipette capacitance C_{P} and a

leakage current through an imperfect seal resistance R_{SEAL} is included in the total current I_{cell} towards the amplifier. To model the effect of extracellular stimulation, the cell membrane with a total surface area of A_{M} is split into two parts. The bottom part resides on top of the PN layer of the OEPC device with a total area of A_{J} and is termed the near cell membrane. The remaining part of the cell membrane with a surface area of $A_{\mathrm{MJ}} = A_{\mathrm{M}} - A_{\mathrm{J}}$ is called the far-cell membrane [39]. In the original two-domain model for external stimulation, the bottom part of the cell membrane is supposed to form a tight seal between the cell membrane is supposed to form a tight seal between the cell and the stimulating electrode [18]. However, for a non-attached cell, the cleft resistance R_{J} is supposed to be much smaller. In addition, the OEPC device in our setup was large compared with the measured cell. We therefore included an additional current I_{OEPC} in the model and the conductivity g_{E} representing the bath resistance towards the ground electrode to account for the rise in potential above the cell, V_{E} (see below). The model in Fig. 2 was implemented in MATLAB/Simulink 2022b. The cell capacitances C_{M} and membrane resistances R_{M} for the respective measurements were estimated based on the approach in [32]. The value for R_J was estimated using a geometry based approach, similar to [29]. The voltage-clamp protocols from the electrophysiological recordings were then fed into the model as V_{cmd} and the results of the output current were filtered by a fourth-order Bessel filter with a corner frequency of 2 kHz, to obtain I_{out} and compared with the measurements. A detailed list of the parameters and their identification can be found in the Appendix.

2) OEPC Equivalent Circuit: We used a photodiode equivalent circuit to model the behavior of the OEPC device (see Fig. 9) [40] in response to light stimulation. The interface to the bath electrolyte was defined as a complex impedance using a weak contribution boundary condition with $R_{\mathrm{f}} = 2.514\ \Omega\mathrm{m}^2$ and $C = 0.1\ \mathrm{F/m}^2$. The PN layer was defined with a size of $A_{\mathrm{PN}} = 6^2\pi = 113.0973\ \mathrm{mm}^2$ and the ITO backelectrode with a size of $A_{\mathrm{ITO}} = 14^2\pi = 615.7522\ \mathrm{mm}^2$. The voltage transients V_{E} and V_{J} above and below the cell (see Fig. 2) for the external stimulation model were determined using a COMSOL-multiphysics simulation of the described equivalent circuit connected to a 2D axisymmetric model of the bath electrolyte with a radius of 15 mm and a conductivity of 1.29 S/m. The electrode contact was modeled flush with the surface of the ITO [41]. The voltage transient V_{E} above the cell in response to a 100 ms $\lambda_{660\ \mathrm{nm}}$ light pulse was measured using current-clamp measurements in $I = 0$ mode right above the cell. However, due to the specifications of the patch amplifier, again, this measured voltage does not fully reproduce the actual voltage transients arising on top of the cell. The speed in $I = 0$ mode of the amplifier generally depends on the time constant of the cell and the pipette resistance R_{p}. Since these measurements were carried out above the cell, R_{M} and C_{M} were assumed to be approximately zero and thus, the rise time was set to 15 μs with 10 % overshoot as described by the manual [38]. Additionally, in current-clamp mode, the electronic gain is twice the selected gain value of the amplifier because of the feedback resistor $R_{\mathrm{f}} = 500\ \mathrm{M}\Omega$. Thus, the output of the current to voltage converter is 0.5 mV/pA. To simplify the scaling task, the headstage output is presented to the user as 1 mV/pA by including an additional two times gain. The voltage V_{J} underneath the cell cannot be measured directly but is assumed to show a slightly higher peak.

III. Results

A. Voltage-Dependent Activation of L-Type Ca^{2+} Current ($I_{Ca,L}$) in Guinea Pig Ventricular Myocyte on OEPC

We have previously characterized steady-state activation of $I_{\mathrm{Ca,L}}$ via voltage-gated $\mathrm{Ca_v}1.2$ channels in Guinea pig ventricular myocytes seeded on glass coverslips [31]. $I_{\mathrm{Ca,L}}$ has a slower activation and inactivation profile than the capacitive transient, which allows us to differentiate and characterize $I_{\mathrm{Ca,L}}$ kinetics. Here, we measured the $I_{\mathrm{Ca,L}}$ activation following the same voltage-clamp protocol in Guinea pig ventricular myocytes seeded on OEPCs. In current density recordings (Fig. 3(a)), depolarizing voltage pulses from -40 mV holding potential for 100 ms indeed produced typical fast inward current activation with maximum amplitude at 0 mV, followed by Ca^{2+}- and voltage-dependent inactivation, as reported earlier on a glass substrate [31]. The current density-voltage relationship (Fig. 3(b)) illustrates a characteristic curve, with a maximum current density of -11.57 ± 0.69 pA/pF at 0 mV and a reversal potential of 49.5 ± 0.96 mV. $I_{\mathrm{Ca,L}}$ conductance plotted as a function of applied voltage (Fig. 3(c)) demonstrates a characteristic sigmoid curve with Boltzmann fit having half maximum activation ($V_{1/2\mathrm{activation}}$) at -10.91 ± 0.65 mV and activation slope of $4.87 \pm 0.23\ \mathrm{mV}^{-1}$.

B. Light-Triggered Activation of $I_{Ca,L}$ in Guinea Pig Ventricular Myocyte on OEPC

Next, we investigated whether endogenous L-type Ca^{2+} channels in the myocytes on OEPC could be activated by photocapacitive charging. 660 nm light ($\lambda_{660\ \mathrm{nm}}$ with 10 mW/mm^2) pulses indeed activated $I_{\mathrm{Ca,L}}$ similar to the conventional voltage step. As illustrated in Fig. 4(a), depolarization from -40 to 0 mV for 100 ms activated $I_{\mathrm{Ca,L}}$, and superfusion with 30 μM nifedipine, an L-type Ca^{2+} channel blocker, largely blocked $I_{\mathrm{Ca,L}}$ as well as the steady-state background current (at the end of the voltage step). Like 0 mV depolarizing voltage step, $\lambda_{660\ \mathrm{nm}}$ pulse at -40 mV for 100 ms (Fig. 4(b)) also induced membrane depolarization sufficient to activate an inward current, which was largely inhibited after nifedipine superfusion, confirming the current as $I_{\mathrm{Ca,L}}$. Although the shape of the residual current after superperfusion with nifedipien in Fig. 4(b) resembles the $I_{\mathrm{Ca,L}}$ traces, it is for the most part the result of the photocapacitive stimulation (see Section D for more details). Fig. 8(c) shows the respective proportion of the transient current and $I_{\mathrm{Ca,L}}$ before and after superperfusion with nifedipine. The nifedipine-sensitive $I_{\mathrm{Ca,L}}$ (Fig. 4(c)), calculated as the difference between current amplitude before and after nifedipine superfusion, was similar between 0 mV and $\lambda_{660\ \mathrm{nm}}$ with 10 mW/mm^2 (10.49 ± 1.46 pA/pF vs. 10.16 ± 1.63 pA/pF). To exclude

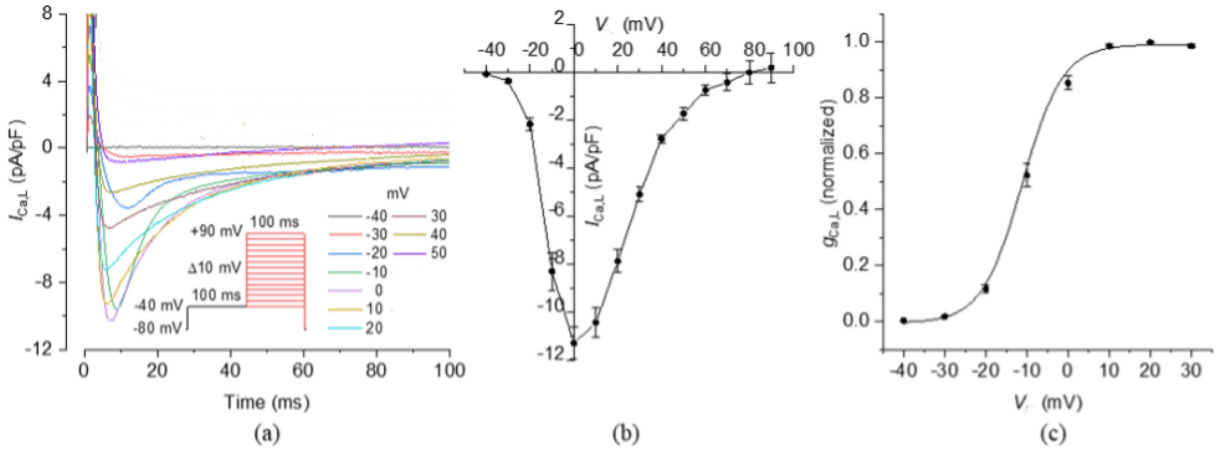

Fig. 3. Voltage-dependent activation of $I_{\mathrm{Ca,L}}$ in Guinea pig ventricular myocyte on OEPC. (a) Representative $I_{\mathrm{Ca,L}}$ recordings of a Guinea pig ventricular myocyte on OEPC during 100 ms voltage pulses (shown in inset) from −40 mV to +90 mV (10 mV interval), preceded by 100 ms prepulse from −80 mV holding potential to −40 mV. (b) $I_{\mathrm{Ca,L}}$ density and (c) steady-state activation of $Ca_v1.2$ channels with Boltzmann fit having half maximum activation ($V_{1/2\mathrm{activation}}$) at −10.91 ± 0.65 mV and activation slope of 4.87 ± 0.23 mV^{-1}; N = 8 cells; mean ± SEM values are shown. *V*: commanded membrane potential, $g_{\mathrm{Ca,L}}$: $I_{\mathrm{Ca,L}}$ conductance.

photothermal activation and artifacts from light pulses, we performed another set of recordings with photothermal devices made of indigo instead of PN as an organic absorber layer. Despite having a similar absorption spectrum to PN, indigo converts the absorbed light into heat instead of capacitive charging [39]. A $\lambda_{660\ \mathrm{nm}}$ light pulse (10 $\mathrm{mW/mm^2}$) for 100 ms failed to activate $I_{\mathrm{Ca,L}}$ (Fig. 4(d)), confirming that the stimulation in PN devices is mainly photocapacitive, with negligible photothermal and photofaradaic effects. We further checked how varying light intensities can modulate $I_{\mathrm{Ca,L}}$. Fig. 4(e) shows $I_{\mathrm{Ca,L}}$ traces activated with varying intensity (1 to 10 $\mathrm{mW/mm^2}$) of the λ_{660} nm pulses. The amplitude of $I_{\mathrm{Ca,L}}$ activation increased progressively from -4.6 ± 0.92 pA/pF to -14.28 ± 1.17 pA/pF with increasing $\lambda_{660\ \mathrm{nm}}$ pulses from 1 to 10 $\mathrm{mW/mm^2}$ (Fig. 4(f)). Fig. A.2 in the Appendix shows the corresponding simulations and the proportion of $I_{\mathrm{Ca,L}}$ for the stimulation with different light intensities. Voltage-dependent and Light-triggered Inactivation of $\mathrm{I_{Ca,L}}$ in Guinea Pig Ventricular Myocyte on OEPC.

We further evaluated the light-triggered steady-state inactivation of $I_{\mathrm{Ca,L}}$ in comparison with voltage-dependent inactivation. Fig. 5(a) and (b) show $I_{\mathrm{Ca,L}}$ recordings for 100 ms at +10 mV voltage pulse and $\lambda_{660\ \mathrm{nm}}$ (10 $\mathrm{mW/mm^2}$) pulse respectively from prepulses of −45 to +10 mV at 5 mV steps. Normalized peak $I_{\mathrm{Ca,L}}$ amplitude plotted as a function of prepulse potential (Fig. 5(c)) illustrates an increase in channel inactivation with increasing prepulse potential from −45 mV to +10 mV. The inactivation curve fitted with the Boltzmann equation showed a membrane potential at half maximum inactivation ($V_{1/2\mathrm{inactivation}}$) at -20.29 ± 0.83 mV and an inactivation slope of 4.17 ± 0.08 $\mathrm{mVs^{-1}}$. A $\lambda_{660\ \mathrm{nm}}$ pulse leads to a similar inactivation curve with Boltzmann fit having $V_{1/2\mathrm{inactivation}}$ at - 20.25 ± 1.17 mV and an inactivation slope of 4.52 ± 0.29 $\mathrm{mVs^{-1}}$. The $V_{1/2\mathrm{inactivation}}$ in Fig. 5(d) was not significantly different between +10 mV voltage step and a $\lambda_{660\mathrm{nm}}$ pulse.

TABLE I
FIXED PARAMETERS USED FOR THE AMPLIFIER AND OEPC EQUIVALENT CIRCUIT

Symbol	Value	Description	Determination
R_f	500 MΩ / 50 MΩ	Feedback resistance of patch-clamp amplifier in β=1 mode and β=0.1, respectively	vendor's manual
C_f	1 pF	Capacitive feedback element in β=1 mode	vendor's manual
LAG (τ_{sum})	1 µs	Corner frequency for filter for CORRECTION signal	setting
τ_{clamp}	1 µs	Amplifier time constant	vendor's manual
C_2	5 pF	Injection capacitance for series resistance compensation	vendor's manual
C_1	1 pF	Injection capacitance for pipette compensation	vendor's manual
g^E	0.13 S	Bath resistance from the top of the cell to the reference electrode	estimation using conductivity of medium/distance
R_J	10 MΩ	Seal resistance cell/OEPC	estimation
I_L	0.0028 A	Current generated in response to light (OEPC equivalent circuit)	estimation
$C_{J,OEPC}$	9.4762 nF	Junction capacitance	estimation
$R_{SH,L}$	1432.2 Ω	Shunt resistance, light on	estimation
$R_{SH,D}$	4310.4*2 Ω	Shunt resistance, light off (dark)	estimation
$R_{S,OEPC}$	10 Ω	Series resistance of OEPC equivalent circuit	estimation
A_M	0.35	Relative amount of near cell membrane	estimation (see [31])
$R_{f,PN}$	2.514 Ωm^2	Faradaic resistivity of PN/bath coupling [Ohm*m^2]	estimation
R_{SEAL}	1 GΩ	Seal resistance between cell membrane and patch pipette	estimation
E_{Vs}	0		Estimation

C. Mathematical Modeling and Simulation

In the first simulations, we assessed the cell and patch-clamp model results comparing the measured currents from Fig. 4(a) with the simulation results. The parameters for the specific simulations are specified in Tables I and II. As illustrated in Fig. 6(a), the voltage-clamp protocols used for the electrophysiological

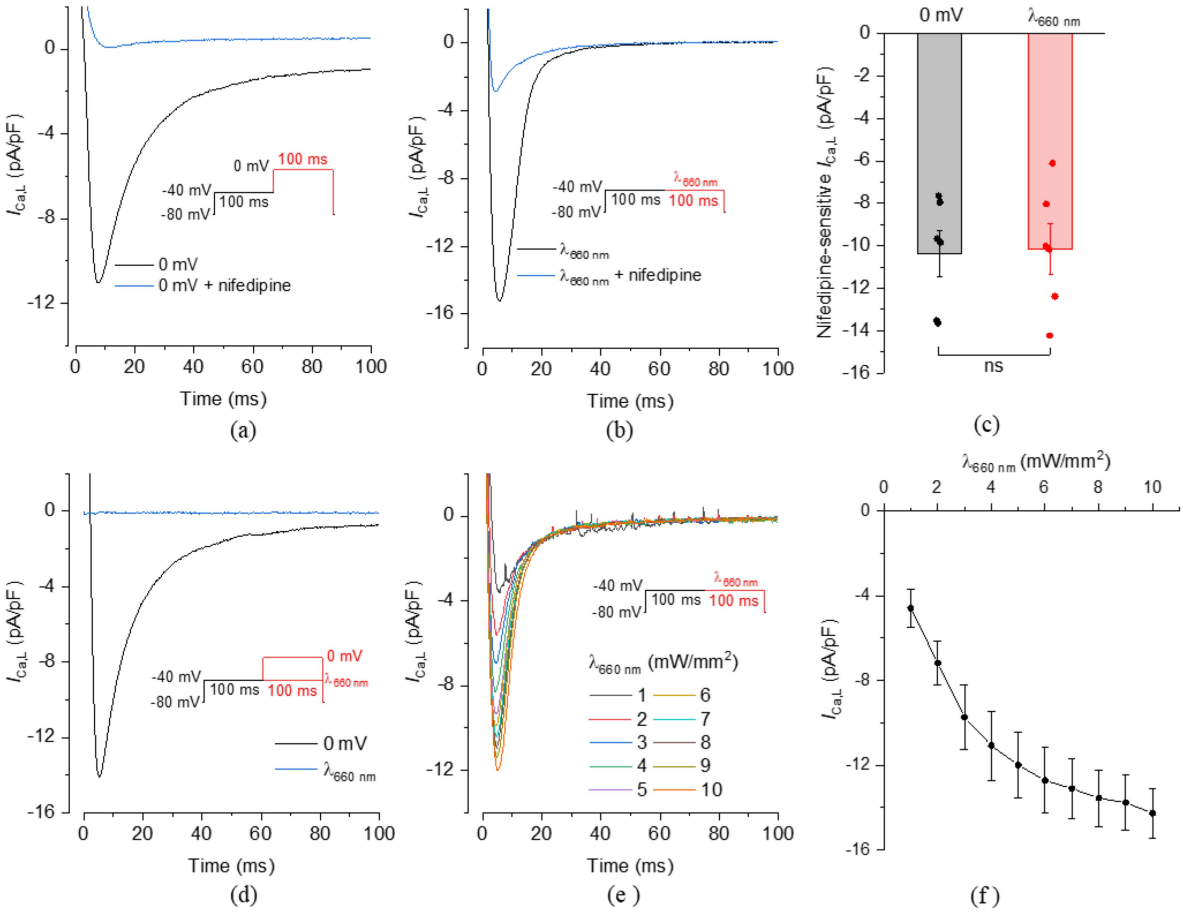

Fig. 4. Light-triggered activation of $I_{\mathrm{Ca,L}}$ in Guinea pig ventricular myocyte on OEPC. Representative $I_{\mathrm{Ca,L}}$ recordings of a Guinea pig ventricular myocyte on OEPC during 100 ms (a) voltage step from -40 mV to 0 mV or (b) 660 nm light ($\lambda_{660\ \mathrm{nm}}$, 10 mW/mm^2) pulse at -40 mV, preceded by 100 ms prepulse from -80 mV holding potential (shown in insets), before and after 1 min superfusion with 30 μM nifedipine. (c) Peak nifedipine-sensitive $I_{\mathrm{Ca,L}}$ density at 0 mV and $\lambda_{660\ \mathrm{nm}}$ light-pulse as shown in (a) and (b) respectively, N $=$ 6 cells. Representative $I_{\mathrm{Ca,L}}$ recordings of a Guinea pig ventricular myocyte on OEPC heat control (indigo) during a 100 ms (d) voltage step from -40 mV to 0 mV or $\lambda_{660\ \mathrm{nm}}$ light-pulse at -40 mV and (e) various $\lambda_{660\ \mathrm{nm}}$ intensities at -40 mV, preceded by a 100 ms prepulse from -80 mV holding potential (shown in insets). (f) Peak $I_{\mathrm{Ca,L}}$ density at various $\lambda_{660\ \mathrm{nm}}$ light intensities shown in (e), N $=$ 5 cells. Mean $\pm$ SEM values are shown; ns: not significant, p $=$ 0.894, unpaired t-test.

recordings were fed into the model as V_{cmd}, and the simulated results of I_{out} were compared with the patch-clamp results. Fig. 6(b) shows a representative simulation result including the capacitive transients from applying a voltage step from -40 mV to 20 mV (Fig. 6(a)) including the whole-cell series resistance compensation with %PREDICTION and %CORRECTION set to 40% comparing the measurement (blue line) with the simulations (black dashed line). Fig. 6(c) shows the respective simulated actual intracellular voltage V_{intra}, which slightly deviates from the V_{cmd} setting due to a non-perfect series resistance compensation, and the simulated correction signal V_{CORR}. Fig. 6(d) shows the 40 % cancellation of the capacitive transients together with the remaining capacitive peak. Fig. 6(e) shows the prediction input signal of the patch-clamp amplifier as described above V_{PRED}.

To simulate the blocking of $I_{\mathrm{Ca,L}}$ with nifedipine superfusion, the permeability of $I_{\mathrm{Ca,L}}$ was decreased to $P_{\mathrm{Ca,nif}} = 0.07\ P_{\mathrm{Ca}}$ and $P_{\mathrm{Na,nif}} = 0$ in the simulations. Fig. 7(a) shows the results of the simulations compared with cell measurements with and without nifedipine for a voltage step to 20 mV. The corresponding simulated voltages V_{intra} are shown in Fig. 7(b). Due to lower current flowing after 1 min superfusion with nifedipine, V_{intra} is closer to the command voltage V_{cmd} and thus the voltage drop accross the series resistance R_{S} is smaller.

Next, light-triggered activation of $I_{\mathrm{Ca,L}}$ was simulated and compared with the patch-clamp measurements in Fig. 8 using the voltage-clamp protocol for the experiments described in Fig. 8(a) and the simulated voltages arising from a 100 ms light pulse. The permeability of $I_{\mathrm{Ca,L}}$ was set to zero for the nifedipine measurements. Fig. 8(b) shows the comparison of the simulated output current I_{out} and the measured cell current in response to light stimulation before and after 1 min superperfusion with nifedipine. To further explain the residual current after superperfusion with nifedipine in Figs. 4(b) and (b), we show the amount of the capacitive transient current as well as the contribution of $I_{\mathrm{Ca,L}}$ to the measured current in Fig. 8(c). As can be seen, the deviations in Fig. 8(b) for the nifedipine traces can be attributed to this transient capacitive stimulation

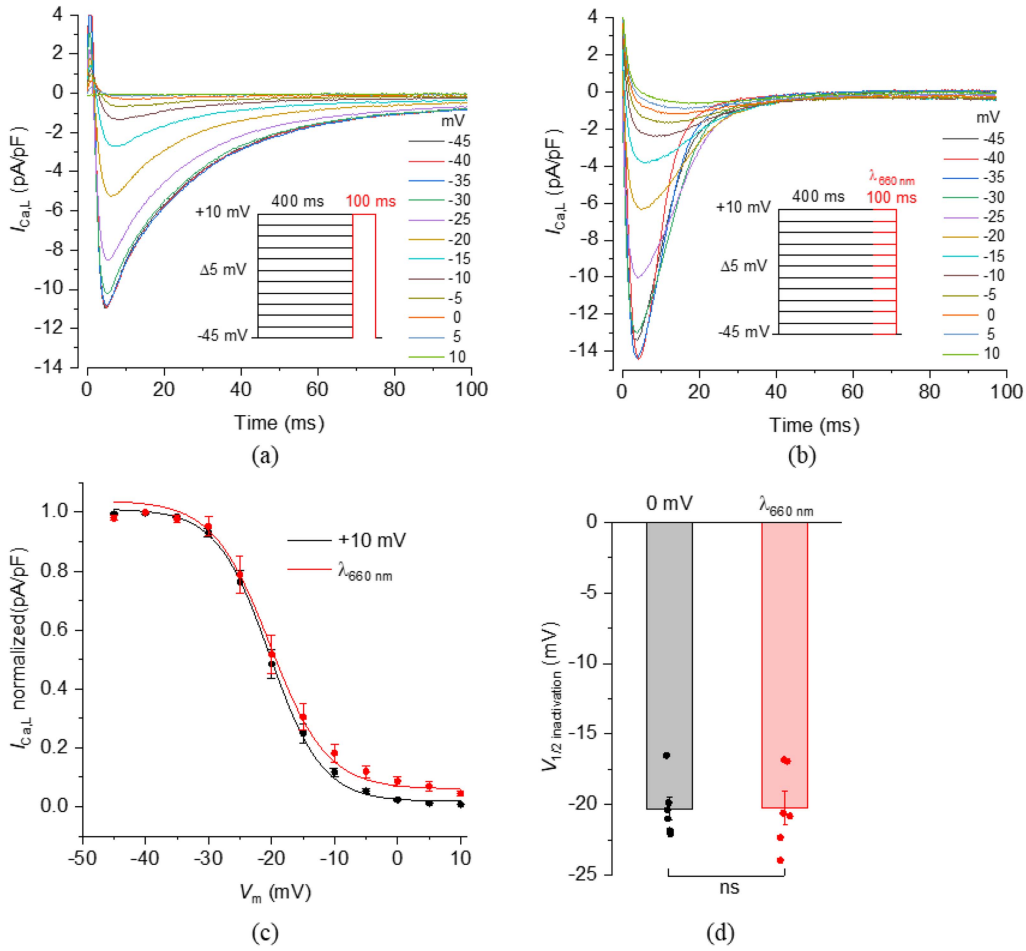

Fig. 5. Voltage-dependent and light-triggered inactivation of $I_{\mathrm{Ca,L}}$ in Guinea pig ventricular myocyte on OEPC. Representative $I_{\mathrm{Ca,L}}$ recordings of a Guinea pig ventricular myocyte on OEPC during 100 ms (a) voltage step to +10 mV and (b) $\lambda_{660\ \mathrm{nm}}$ pulse (10 mW/mm^2), preceded by conditioning prepulses from −45 to +10 mV (5 mV increment, 400 ms) as shown in the insets. (c) steady-state inactivation of $Ca_v1.2$ channels showing Boltzmann fit for normalized peak amplitude of $I_{\mathrm{Ca,L}}$ as a function of prepulse commanded membrane potential (V) and (d) membrane potential at half maximum inactivation ($V_{1/2\mathrm{inactivation}}$) for +10 mV and $\lambda_{660\ \mathrm{nm}}$; N = 6; mean ± SEM values are shown; ns: not significant, p = 0.978, unpaired t-test.

TABLE II
PARAMETERS FOR THE DIFFERENT SIMULATIONS

Symbol	Value Fig. 6	Value Fig. 7/8	Description	Determination
C_P	5 pF	5 pF	Pipette capacitance	estimation
R_P	2.5 MΩ	2.5 MΩ	Pipette resistance	measurement
R_P*	2.5 MΩ	2.5 MΩ	Estimated pipette resistance	setting/estimation
C_P*	5 pF	5 pF	Estimated pipette capacitance	setting/estimation
C_M	143.4 pF	139 pF	Membrane capacitance (100 - 150 pF)	estimation [25]
R_M	220 MΩ	554.2MΩ	Membrane resistance	estimation [25]
R_S	7.4 MΩ	9.41 MΩ	Series resistance	estimation [25]
C_M*	100 pF	100 pF	Estimated membrane capacitance (0.3 – 100 pF in β=1 mode)	setting/estimation
R_S*	7.4 MΩ	15.5 MΩ	Estimated series resistance	setting/estimation
% CORRECTION	0.35	0.3	Amount of compensation for voltage drops across R_S (0 - 100)	setting/estimation
% PREDICTION	0.35	0.3	Amount of compensation for loading delay of membrane potential V_m(0 - 100)	setting/estimation

artifact current. The corresponding simulated voltages V_{intra} are depicted in Fig. 8(d), again before and after superperfusion with nifedipine. We observe that after superperfusion with nifedipine, thus blocking $I_{\mathrm{Ca,L}}$ and decreasing the conductivity of the cellular membrane, the intracellular voltage is slightly higher, an effect that could also be observed previously comparing the intracellular voltage with and without expression of voltage-gated channels. We need to state that, as in previous studies [23], the voltage V_{intra} describes the potential difference between the patch-clamp electrode and a distant reference electrode as measured and controlled by the patch-clamp amplifier (see Fig. 2) and does not correspond to the actual membrane voltage of the measured cell, which is, in this configuration, location dependent. However, V_{intra} reflects the transient change in the intracellular potential in response to the external stimulation and can be used to describe differences in the effect of the external stimulation on the cell for different experimental settings. For example, to assess the effect of the patch-clamp amplifier on the measured current, we compared the results for different amounts of whole-cell series resistance compensation on the measurement outcome and the respective intracellular voltage in Fig. 8(f) and (g). The OEPC response to a light-pulse was simulated using the equivalent circuit representation in Fig. 9.

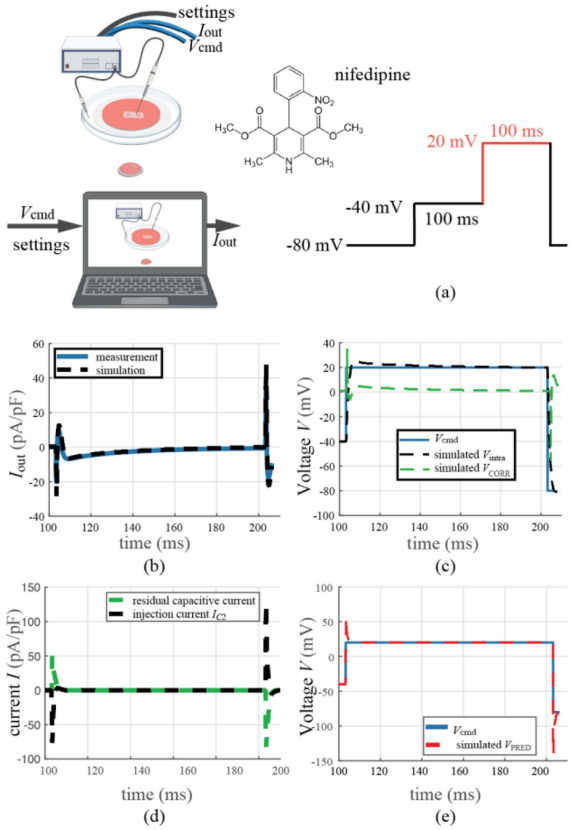

Fig. 6. Modeling results for voltage-clamp activation of $I_{Ca,L}$: (a) Applied command voltage V_{cmd}. The red parts of the trace are shown. (b) Representative $I_{Ca,L}$ recording (blue solid line) during a 100 ms voltage pulse from −40 mV to +20 mV, preceded by 100 ms prepulse from −80 mV holding potential to −40 mV and respective simulation result (dashed black line) (c). Simulated potential V_{intra} (dashed black line) in comparison to the applied command voltage V_{cmd} and the assumed correction signal V_{CORR}. (d) Estimated injected current over the injection capacitance C_2 and remaining capacitive transient. (e) Simulated prediction signal V_{PRED} in comparison to the applied command voltage V_{cmd}.

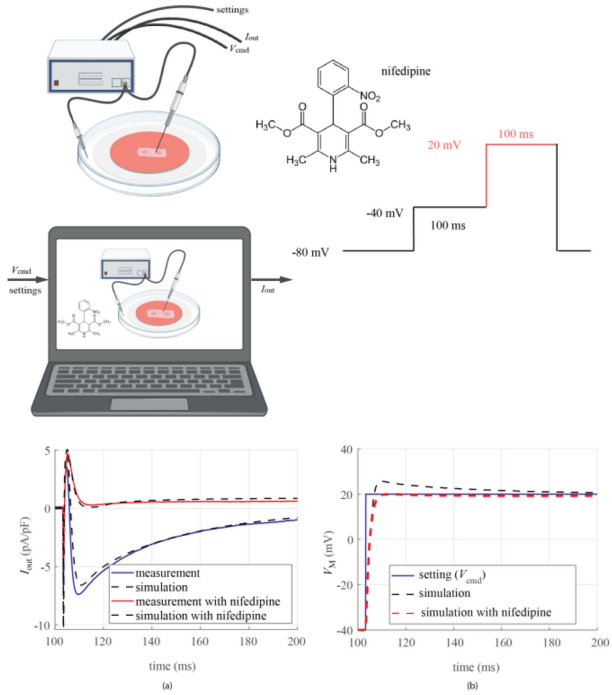

Fig. 7. Nifedipine sensitivity. (a) Comparison of a representative $I_{Ca,L}$ recording of a Guinea pig ventricular myocyte on OEPC during a 100 ms voltage step from −40 mV to 20 mV preceded by 100 ms prepulse from −80 mV holding potential (as shown in Fig. 6(a)), before and after 1 min superfusion with 30 μM nifedipine with the simulation results (dashed lines). (b) Corresponding simulated membrane voltages before and after superperfusion with nifedipine. Due to a much lower current after nifedipine superperfusion, the effect of R_S is smaller.

The voltage V_E (see equivalent circuit in Fig. 2) above the cell upon a 100 ms $\lambda_{660\ nm}$ light pulse was measured using current-clamp measurements in $I = 0$ mode right above the cell and compared with the modeling result (dashed line) taking the specifications of the patch-clamp amplifier in current-clamp mode as well as the filtering of the amplifier into account. Fig. 8(e) shows a comparison of the simulated and the measured voltage V_E above the cell.

IV. Discussion

The present study evaluates OEPCs as extracellular, wireless stimulation electrodes driven by red light pulses to activate endogenous voltage-gated Ca^{2+} channels in isolated cardiac myocytes. Cardiac myocytes provide a valuable in vitro model to mimic *in vivo* photostimulation of native ion channels of non-attached, excitable cells on top of the OEPC device. Our findings have several implications and provide valuable insights into the functionality and applicability of OEPC devices in electrophysiological experiments. First, our results indicate that the presence of the OEPC surface does not significantly influence native activation and inactivation characteristics of voltage-gated Ca^{2+} channels during voltage-clamp recordings of cardiac myocytes compared with a glass surface [23].

Furthermore, our study demonstrates that red light pulses activating the OEPCs successfully stimulate cardiac myocytes, resulting in the elicitation of nifedipine-sensitive $I_{Ca,L}$. The activation and inactivation profiles of the light-induced $I_{Ca,L}$ activation on PN-based OEPCs are comparable with those observed in voltage-dependent activation during standard voltage-clamp recordings. Importantly, we show that the observed activation is mainly photocapacitive and not photothermal, as indigo-based devices that convert absorbed light into heat failed to elicit $I_{Ca,L}$ in cardiac myocytes. The results are in line with our previous in vitro findings, which demonstrated light-triggered membrane depolarization sufficient to activate voltage-gated K^+ channels in *Xenopus laevis* oocytes and HEK293 cells [15], [23], [39]. The consistency of our findings across different cell types further supports the reliability and reproducibility of the observed effects.

The modeling and simulation results reproduce the measured currents from the voltage-clamp experiments and allow us to analyze the achievable intracellular voltage levels in response to OEPC stimulation at the same time. In contrast to previous studies modeling the effect of external stimulation on cellular

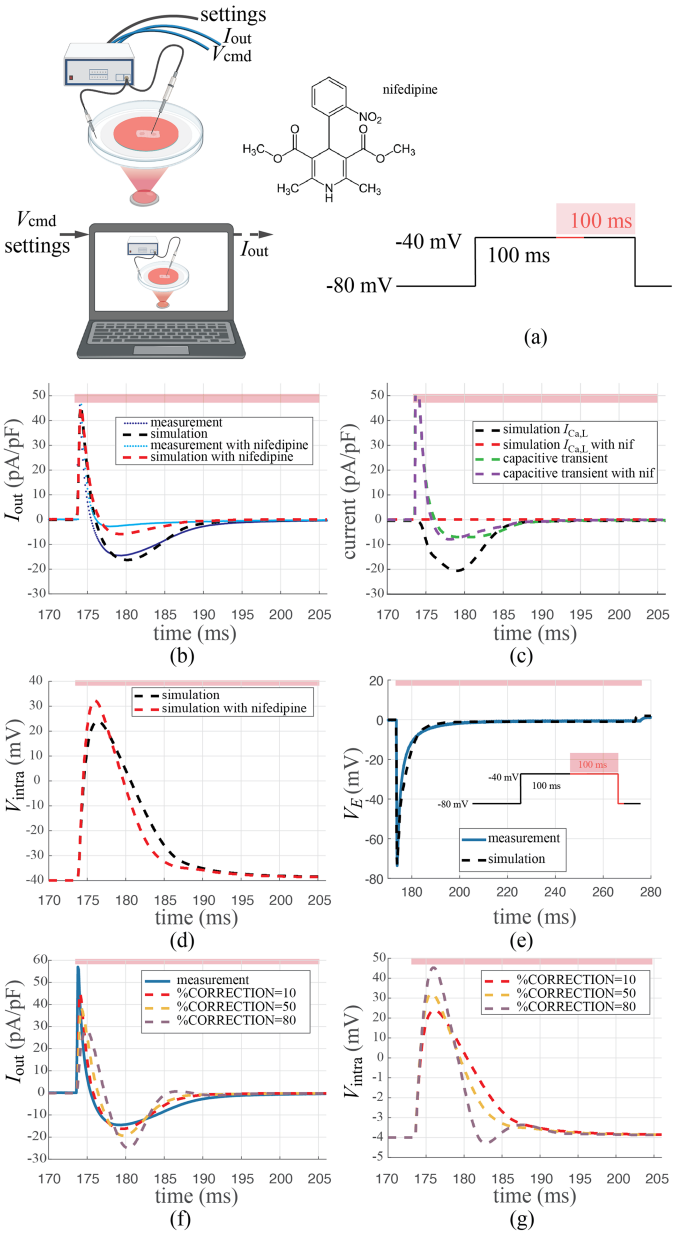

Fig. 8. Simulation results of light-triggered activation of $I_{Ca,L}$ in Guinea pig ventricular myocyte on OEPCs. The red colored bar on top of the traces correspond to the time where the LED is on. (a) Applied command voltage $V_{cmd.}$ (b) Representative current recordings of a Guinea pig ventricular myocyte on OEPC for a 100 ms light pulse ($\lambda_{660\ nm}$, 10 mW/mm^2) at -40 mV, preceded by a prepulse from -80 mV holding potential, before and after 1 min superfusion with 30 μM nifedipine and respective simulation results (dashed lines). (c) respective contribution of $I_{Ca,L}$ and the capacitive transient currents in response to stimulation before and after superperfusion with nifedipine. (d) Corresponding simulated voltages $V_{intra.}$ (e) Representative measurement of the voltage above the cell V_E and simulation result of the OEPC equivalent circuit (dashed line). (f,g) Simulated current I_{out} and simulated achieved intracellular voltage levels V_{intra} in response to external stimulation for different settings of the amplifier's compensation circuit.

behavior [36], we focus here on a rather detailed description of the cell's ion channel kinetics and introduce a model for a large stimulation device in comparison to the cell size. The results emphasize the significance of considering the specific ion channels activated within the cell when comparing absolute

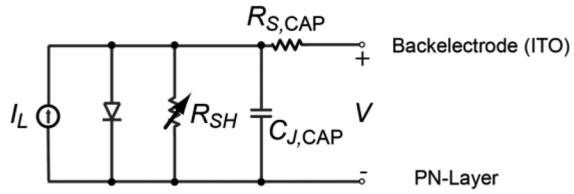

Fig. 9. Equivalent circuit model for the OEPC device. The ideal current source I_L represents the current generated by the photodevice in response to light. $C_{J,OEPC}$ represents the junction capacitance and R_{SH} the shunt resistance, which takes on different values in the light or in the dark. $R_{S,OEPC}$ is the series resistance.

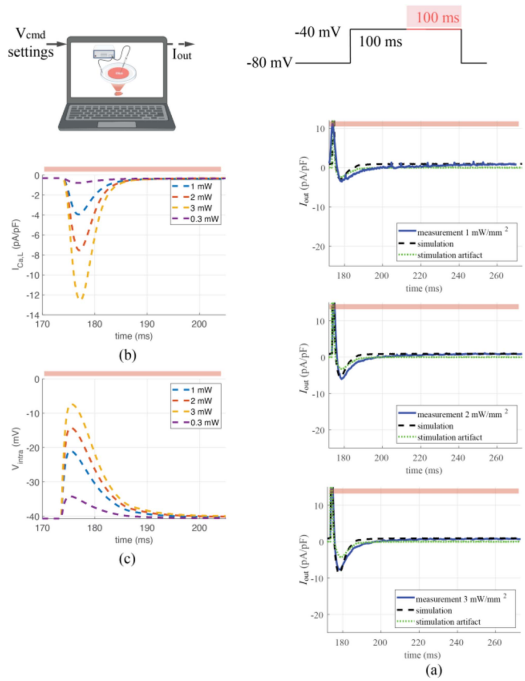

Fig. 10. (a) Comparison of measured and simulated currents I_{out} at different light intensities and the transient current which results from the OEPC stimulation for 1 mW/mm^2 (top), (b) 2 mW/mm^2 and (c) 3 mW/mm^2 (bottom). (b) Simulated contribution of $I_{Ca,L}$ for the respective measurements in (a). Extrapolation of the model to 0.3 mW/mm^2. (c) Corresponding simulated achievable intracellular potential for the respective traces in (a) and the extrapolated simulation for 0.3 mW/mm^2.

external stimulation results between different cell types and ion channels present in the cellular membrane. In addition, the model allows us to discriminate between the artifact current arising from the external stimulation through the OEPC device and the actual amount of nifedipine sensitive $I_{Ca,L}$ current. In voltage-clamp experiments, the voltage V_{intra} corresponds mainly to the membrane voltage of the cell and is actively held at a specific potential by the voltage-clamp amplifier. In our light stimulation experiments, V_{intra} does not reflect the voltage drop across the cellular membrane, but still describes the potential as controlled by the patch-clamp amplifier and is characteristic of OEPC devices at the beginning of the stimulation pulse leading to light-induced membrane depolarization. Presenting V_{intra} allows for a direct comparison with other relevant research where this quantity has been employed.

The modeling and simulation results obtained in this study provide insights into the voltage levels achieved in response to OEPC stimulation and introduce a model for a large stimulation device in comparison with the cell size. This close interaction of the two devices affecting the intracellular potential hinders the isolation of the impact of the external stimulation, unless the response of the voltage-clamp amplifier is taken into account. By incorporating the amplifier's response characteristics and compensation mechanism, we were able to simulate the interplay between the external stimulation device and the amplifier's compensatory mechanisms [26] providing a more realistic representation of the experimental conditions and enabling a more accurate assessment of the specific contributions to the recorded membrane currents.

V. Conclusion

Overall, our findings provide evidence for the efficacy of wireless OEPCs as extracellular photostimulation electrodes to study the complex kinetics of voltage-gated ion channels in isolated, excitable cells. The ability to achieve precise control and activation of membrane currents through external stimulation while simultaneously using the patch-clamp technique opens up possibilities for investigating the functional properties and dynamics of ion channels in various biological systems [39], [14], [24], [25]. OEPCs offer a wireless, in vitro electrophysiology tool for biophysicists and further insights into potential *in vivo* photostimulation of physiological processes in a minimally invasive manner. Our computational model highlights the significance of incorporating a model of the voltage-clamp amplifier when investigating the effects of external stimulation on membrane currents and voltages providing insights into the combined impact of the stimulation and the amplifier's compensatory actions. This leads to a more thorough understanding of the experimental outcomes and their interpretation, advancing our knowledge of ion channel modulation in response to external stimulation.

Acknowledgment

The authors thank Eric Daniel Glowacki, Karin Kornmueller, and Marta Nowakowska for their expertise and assistance throughout the study.

References

[1] V. A. Pavlov and K. J. Tracey, "Bioelectronic medicine: Updates, challenges and paths forward," *Bioelectron. Med.*, vol. 5, no. 1, Dec. 2019, Art. no. 1.

[2] M. I. Muzquiz et al., "In-vivo application of low frequency alternating currents on porcine cervical vagus nerve evokes reversible nerve conduction block," *Bioelectron. Med.*, vol. 7, no. 1, Dec. 2021, Art. no. 9.

[3] A. Khalifa et al., "Injectable wireless microdevices: Challenges and opportunities," *Bioelectron. Med.*, vol. 7, no. 1, Dec. 2021, Art. no. 19.

[4] H. Knotkova et al., "Neuromodulation for chronic pain," *Lancet*, vol. 397, no. 10289, pp. 2111–2124, May 2021.

[5] S. Kim, H. Roh, and M. Im, "Artificial visual information produced by retinal prostheses," *Front. Cellular Neurosci.*, vol. 16, Jun. 2022, Art. no. 911754, doi: 10.3389/fncel.2022.911754.

[6] D. Ziesel et al., "Electrical stimulation methods and protocols for the treatment of traumatic brain injury: A critical review of preclinical research," *J. NeuroEngineering Rehabil.*, vol. 20, no. 1, Apr. 2023, Art. no. 51.

[7] E. Katz, "Implantable bioelectronics-Ed.ial introduction," in *Implantable Bioelectronics*, E. Katz Ed. Weinheim, Germany: Wiley, 2014, pp. 1–5.

[8] K. Iniewski, "Introduction to biosensors," in *Handbook of Bioelectronics: Directly Interfacing Electronics and Biological Systems*. S. Carrara and K. Iniewski Eds. Cambridge, U.K., MA, USA: Cambridge Univ. Press, 2015. pp. 105–108.

[9] R. Parameswaran et al., "Optical stimulation of cardiac cells with a polymer-supported silicon nanowire matrix," *Proc. Nat. Acad. Sci. United States Amer.*, vol. 116, no. 2, pp. 413–421, Jan. 2019, doi: 10.1073/pnas.1816428115.

[10] M. W. Jenkins et al., "Optical pacing of the embryonic heart," *Nature Photon.*, vol. 4, no. 9, pp. 623–626, Sep. 2010, doi: 10.1038/nphoton.2010.166.

[11] V. Emiliani et al., "Optogenetics for light control of biological systems," *Nature Rev. Methods Primers*, vol. 2, no. 1, Jul. 2022, Art.no. 55.

[12] K. Mathieson et al., "Photovoltaic retinal prosthesis with high pixel density," *Nature Photon.*, vol. 6, no. 6, pp. 391–397, Jun. 2012.

[13] T. D. Y. Kozai et al., "Brain tissue responses to neural implants impact signal sensitivity and intervention strategies," *ACS Chem. Neurosci.*, vol. 6, no. 1, pp. 48–67, Jan. 2015.

[14] R. David et al., "Direct electrical neurostimulation with organic pigment photocapacitors," *Adv. Mater.*, vol. 9, May 2018, Art. no. 1707292.

[15] M. Jakešová et al., "Optoelectronic control of single cells using organic photocapacitors," *Sci. Adv.*, vol. 5, no. 4, Apr. 2019, Art. no. eaav5265.

[16] M. Warczak et al., "Organic semiconductor perylenetetracarboxylic diimide (PTCDI) electrodes for electrocatalytic reduction of oxygen to hydrogen peroxide," *Chem. Commun.*, vol. 54, no. 1, pp. 1960–1963, 2018.

[17] P. Fromherz, "Semiconductor chips with ion channels, nerve cells and brain," *Physica E: Low-dimensional Syst. Nanostructures*, vol. 16, no. 1, pp. 24–34, Jan. 2003, doi: 10.1016/S1386-9477(02)00578-7.

[18] I. Schoen and P. Fromherz, "The mechanism of extracellular stimulation of nerve cells on an electrolyte-oxide-semiconductor capacitor," *Biophysical J.*, vol. 92, no. 3, pp. 1096–1111, Feb. 2007, doi: 10.1529/biophysj.106.094763.

[19] T. Schmidt et al., "Light stimulation of neurons on organic photocapacitors induces action potentials with millisecond precision," *Adv. Mater. Technol.*, vol. 7, no. 9, Sep. 2022, Art. no. 2101159, doi: 10.1002/admt.202101159.

[20] L. Steven, "Corrigendum: Optical properties of biological tissues: A review," *Phys. Med. Biol.*, vol. 58, no. 14, Jun. 2013, Art. no. 5007, doi: 10.1088/0031-9155/58/14/5007.

[21] V. Đerek et al., "Untangling photofaradaic and photocapacitive effects in organic optoelectronic stimulation devices," *Front. Bioeng. Biotechnol.*, vol. 8, 2020, Art. no. 284, [Online]. Available: https://www.frontiersin.org/articles/10.3389/fbioe.2020.00284

[22] J. Ehlich et al., "Direct measurement of oxygen reduction reactions at neurostimulation electrodes," *J. Neural Eng.*, vol. 19, no. 3, Jun. 2022, Art. no. 036045, doi: 10.1088/1741-2552/ac77c0.

[23] M. S. Ejneby et al., "Extracellular photovoltage clamp using conducting polymer-modified organic photocapacitors," *Adv. Mater. Technol.*, vol. 5, no. 3, Mar. 2020, Art. no. 1900860, doi: 10.1002/admt.201900860.

[24] M. S. Ejneby et al., "Chronic electrical stimulation of peripheral nerves via deep-red light transduced by an implanted organic photocapacitor," *Nature Biomed. Eng.*, vol. 6, no. 6, pp. 741–753, Jun. 2022, doi: 10.1038/s41551-021-00817-7.

[25] F. Missey et al., "Organic electrolytic photocapacitors for stimulation of the mouse somatosensory cortex," *J. Neural Eng.*, vol. 18, no. 6, Nov. 2021, Art. no. 066016, doi: 10.1088/1741-2552/ac37a6.

[26] O. S. Abdullaeva et al., "Organic photovoltaic sensors for photocapacitive stimulation of voltage-gated ion channels in neuroblastoma cells," *Adv. Funct. Mater.*, vol. 29, no. 21, May 2019, Art. no. 1805177, doi: 10.1002/adfm.201805177.

[27] F. G. Cosi et al., "Multiscale modeling of dyadic structure-function relation in ventricular cardiac myocytes," *Biophysical J.*, vol. 117, no. 12, pp. 2409–2419, Dec. 2019, doi: 10.1016/j.bpj.2019.09.023.

[28] M. A. Colman et al., "Multi-scale computational modeling of spatial calcium handling from nanodomain to whole-heart: Overview and perspectives," *Front. Physiol.*, vol. 13, Mar. 2022, Art. no. 836622, doi: 10.3389/fphys.2022.836622.

[29] M. Polz et al., "Holistic equivalent circuit model for capacitive extracellular stimulation," *J. Curr. Directions Biomed. Eng.*, vol. 8, no. 2, pp. 777–780, 2022, doi: 10.1515/cdbme-2022-1198.

[30] C. L. Lei et al., "Accounting for variability in ion current recordings using a mathematical model of artefacts in voltage-clamp experiments," *Philos. Trans. Roy. Soc. A: Math., Phys. Eng. Sci.*, vol. 378, no. 2173, May 2020, Art. no. 20190348, doi: 10.1098/rsta.2019.0348.

[31] C. N. Koyani et al., "Dipeptidyl peptidase-4 independent cardiac dysfunction links saxagliptin to heart failure," *Biochem. Pharmacol.*, vol. 145, pp. 64–80, Dec. 2017, doi: 10.1016/j.bcp.2017.08.021.

[32] D. Platzer and K. Zorn-Pauly, "Accuracy considerations for capacitance estimation by voltage steps in cardiomyocytes," *Prog. Biophys. Mol. Biol.*, vol. 157, pp. 3–10, Nov. 2020, doi: 10.1016/j.pbiomolbio.2020.03.001.

[33] G. M. Faber et al., "Kinetic properties of the cardiac L-type Ca2+ channel and its role in myocyte electrophysiology: A theoretical investigation," *Biophysical J.*, vol. 92, no. 5, pp. 1522–1543, Mar. 2007, doi: 10.1529/biophysj.106.088807.

[34] A. Agrawal et al., "Models of the cardiac L-type calcium current: A quantitative review," *WIREs Mechanisms Dis.*, vol. 15, no. 1, Jan. 2023, Art. no. e1581, doi: 10.1002/wsbm.1581.

[35] S. Langthaler et al., "Ion channel modeling beyond state of the art: A comparison with a system theory-based model of the shaker-related voltage-gated potassium channel Kv1.1," *Cells*, vol. 11, no. 2, Jan. 2022, Art. no. 239, doi: 10.3390/cells11020239.

[36] A. Agrawal et al., "Models of the cardiac L-type calcium current: A quantitative review," *WIREs Mechanisms Dis.*, vol. 15, Jan. 2022, Art. no. e1581, doi: 10.1101/2021.10.04.462988.

[37] C. H. Luo and Y. Rudy, "A dynamic model of the cardiac ventricular action potential. I. Simulations of ionic currents and concentration changes," *Circulation Res.*, vol. 74, no. 6, pp. 1071–1096, Jun. 1994, doi: 10.1161/01.RES.74.6.1071.

[38] *Axopatch 200B Patch Clamp Theory and Operation Part Number 2500-121 Rev D*. Union City, CA, USA: Axon Instrum., Inc, 1999.

[39] T. Schmidt et al., "Light stimulation of neurons on organic photocapacitors induces action potentials with millisecond precision," *Adv. Mater. Technol.*, vol. 31, Mar. 2022, Art. no. 2101159, doi: 10.1002/admt.202101159.

[40] J. H. Chuah and D. Holburn, "Design of pixellated CMOS photon detector for secondary electron detection in the scanning electron microscope," *Adv. Optoelectron.*, vol. 2011, Jun. 2011, Art. no. 648487, doi: 10.1155/2011/648487.

[41] N. A. Pelot, B. J. Thio, and W. M. Grill, "Modeling current sources for neural stimulation in COMSOL," *Front. Comput. Neurosci.*, vol. 12, Jun. 2018, Art. no. 40, doi: 10.3389/fncom.2018.00040.